CORA Cork Open Research Archive
Cartlann Taighde Oscailte Chorcaí

Title	Loxodromes in open multisection lasers
Authors	O'Connor, Christopher P. J.;Wieczorek, Sebastian;Amann, Andreas
Publication date	2023-05-26
Original Citation	O'Connor, C. P. J., Wieczorek, S. and Amann, A. (2023) 'Loxodromes in open multisection lasers', Physical Review A, 107(5), 053520 (12pp). doi: 10.1103/PhysRevA.107.053520
Type of publication	Article (peer-reviewed)
Link to publisher's version	10.1103/physreva.107.053520
Rights	© 2023, American Physical Society. All rights reserved.
Download date	2026-11-06 11:34:23
Item downloaded from	https://hdl.handle.net/10468/14700

UCC
University College Cork, Ireland
Coláiste na hOllscoile Corcaigh

Loxodromes in Open Multi-Section Lasers

Christopher P. J. O'Connor,[1] Sebastian Wieczorek,[1] and Andreas Amann[1]
[1] *School of Mathematical Sciences, University College Cork, Ireland*

We introduce a formalism to efficiently calculate lasing modes and optical power flow in multi-section lasers with open boundaries. The formalism is underpinned by a projection of the complex-valued electric field and its spatial derivative onto a suitably extended complex $\mathcal{Z}$-plane, to reduce the order of the problem and simplify analysis. In a single-section laser, we show that a laser mode is a *loxodrome* on the extended complex $\mathcal{Z}$-plane. In a multi-section laser, we obtain loxodromes for individual sections of the laser. Then, a multi-section mode is constructed by continuously concatenating individual loxodromes from each section using the open boundary conditions. A natural visualization of this construction is given by stereographic projection of the extended complex $\mathcal{Z}$-plane onto the Riemann sphere. Our formalism simplifies analysis of lasing modes in open multi-section lasers and provides new insight into the mode geometry and degeneracy.

PACS numbers: 42.55.-f,42.60.Da, 03.50.De,41.20.-q

I. INTRODUCTION

With increasing miniaturisation in optical devices and the development of photonic integrated circuits, the problem of modelling optical modes in complex configurations comprising of both active-medium and absorbing sections becomes prominent. For a one-dimensional structure, the core of the problem is to find the solution to a multi-point boundary value problem for the electromagnetic wave equation with complex coefficients, where open boundary conditions complicate the situation. While the single section case, which corresponds to the classical Fabry-Perot laser, can be solved analytically [1], the case of two or more sections is considerably more difficult, but also much more interesting.

The aim of this paper is to give a general method for finding lasing modes in multi-section lasers with open boundaries, and provide a greater intuitive understanding of the geometry of lasing modes. To this end, we propose a formalism outlined in Fig. 1 for laser structures in one spatial dimension denoted z. In the first step, we use the single-mode approximation to reduce the real-valued partial differential wave equation for the electric field $\mathcal{E}(z,t)$ to a complex-valued ordinary differential wave equation for the mode profiles $E(z)$. Since the reduced wave equation is of second-order, the lasing field at each point in space is represented by two complex numbers: the electric field $kE(z)$ and its space derivative $E'(z)$. Hence, a lasing mode is represented by a curve in the two-dimensional complex-valued vector space (four-dimensional real-valued vector space), which is rather difficult to visualize. In consequence, the effects of changing the pump and different laser designs are difficult to understand. In the second step, we address this problem of high dimensionality by a non-invertible H-projection of the two complex-valued variables onto a single complex-valued variable $\mathcal{Z}(z)$, with the origin of the complex E-plane mapped onto infinity of $\mathcal{Z}$. The key idea is that this new variable, in conjunction with stereographic projection, provides a natural representation of a lasing mode as a one-dimensional curve on the *Riemann sphere* [2]. Note that the Riemann sphere has been used successfully in many areas of physics, for example in the guise of the Bloch Sphere representation [3] of a two-level system in quantum computing, or to represent the polarization states of light on the Poincaré sphere [4]. The final step of our formalism is to compute this curve on the Riemann sphere. To this end, we use the elegant mathematical formalism of the (invertible) Möbius transformation [2] to show that:

(i) Each part of a lasing mode in a given section of a multi-section laser is simply a logarithmic spiral on an extended complex plane.

(ii) The inverse Möbius transformation of this logarithmic spiral gives a $\mathcal{Z}(z)$ that corresponds to a special curve on the Riemann sphere called a *loxodrome* [5].

(iii) The entire lasing mode of a multi-section laser with open boundaries is obtained by concatenating individual loxodromes on the Riemann sphere.

A usual approach to obtaining lasing modes in multi-section lasers is the *transfer matrix* approach [6–8]. In this approach, a part of a lasing mode in a given section of a multi-section laser is represented as a complex 2×2 matrix that depends on the physical properties of this section. Our approach reduces the dimensionality of the problem from four to two real dimensions, and thus provides a simpler and more accessible visual representation of lasing modes. This makes it an interesting alternative to the transfer matrix approach.

In order to validate and demonstrate the usefulness of our approach, we first reproduce the well known results for a single-section Fabry-Perot laser. We then study the case of a laser with two sections of the same physical length but with different gain or absorption characteristics. In this case, we distinguish the two options where either both sections have net local gain or, alternatively, one section has net local gain while the other section has net local absorption. By "local" we mean the property

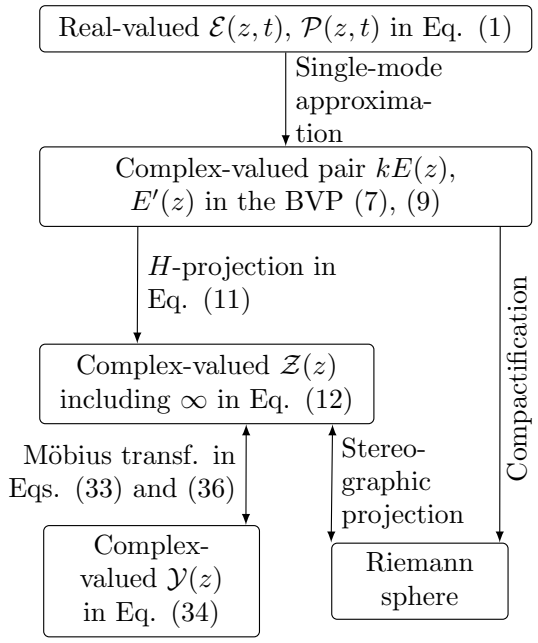


FIG. 1. High level overview of our formalism, including different transformations involved in the three steps discussed in the text.

of the medium excluding boundaries. Finally we study a three-section laser, in which we introduce an air gap between the two outer sections with net local gain.

In this context, we focus on the interesting situations where two different modes coalesce, or become degenerate, upon varying one or two system parameters.

II. ELECTROMAGNETIC WAVE EQUATION

The electric field inside a laser is a three-dimensional real-valued vector that varies in space and time. Consider the spatio-temporal evolution of a single (scalar) component $\mathcal{E}(z,t)$ of this field that varies in the longitudinal z-direction along the laser structure [9]

$$\frac{\partial^2}{\partial z^2}\mathcal{E}(z,t) - \frac{1}{c^2}\frac{\partial^2}{\partial t^2}\mathcal{E}(z,t) - \mu_0\frac{\partial^2}{\partial t^2}\mathcal{P}(z,t) = 0, \quad (1)$$

where c is the speed of light in vacuum, μ_0 is the vacuum permeability, and $\mathcal{P}(z,t)$ is the total real-valued polarisation, which is comprised of both the active medium and background polarisation components. We use a single-mode constant-intensity approximation, and decompose the electric field and polarisation in terms of complex-valued spatial mode profiles, denoted by $E(z)$ and $P(z)$, and temporal oscillations at an optical frequency ω:

$$\mathcal{E}(z,t) = \mathrm{Re}\left[E(z)e^{-i\omega t}\right], \quad (2)$$

$$\mathcal{P}(z,t) = \mathrm{Re}\left[P(z)e^{-i\omega t}\right]. \quad (3)$$

We can now relate the same frequency components of the complex-valued polarisation and electric field [9, 10] by

$$P(z) = \epsilon_0\left(\chi_b(z) + \chi_g(z)\right)E(z), \quad (4)$$

where $\chi_b(z)$ and $\chi_g(z)$ are the complex-valued background and active-medium susceptibilities, respectively. It is useful to introduce the complex-valued permittivity of the medium $\epsilon(z)$:

$$\epsilon(z) = 1 + \chi_b(z) + \chi_g(z). \quad (5)$$

The case of $\mathrm{Im}\left[\epsilon(z)\right] > 0$ corresponds to net local absorption, while $\mathrm{Im}\left[\epsilon(z)\right] < 0$ indicates net local gain or absorption. This allows us to rewrite the wave equation (1) in the succinct form

$$\left(\frac{d^2}{dz^2} + k^2\,\epsilon(z)\right)E(z) = 0, \quad (6)$$

where $k = \omega/c$ is the free-space wavenumber. This second-order differential equation can be written as two coupled first-order differential equations by introducing a new variable $E'(z)$:

$$\begin{aligned}\frac{d}{dz}E(z) &= E'(z),\\ \frac{d}{dz}E'(z) &= -k^2\,\epsilon(z)\,E(z).\end{aligned} \quad (7)$$

Since $E(z)$ and $E'(z)$ are complex-valued, we are dealing with a four-dimensional problem in real variables. This is the first step shown in Fig. 1, in which we move from the real-valued $\mathcal{E}(z,t)$ and $\mathcal{P}(z,t)$ to the complex-valued pair $kE(z)$ and $E'(z)$.

A. Boundary Conditions

In this paper, we consider three different laser structures shown in Fig. 2. The outer boundaries of each laser structure are at $z = 0$ and $z = L$, and we assume only outgoing light at each outer boundary, meaning the light propagates to the left for $z < 0$ and to the right for $z > L$. Assuming vacuum outside the laser structure, we have $\epsilon(z) = 1$ for $z < 0$ and $z > L$. Then, solving Eq. (6) under the outgoing light assumption gives

$$E(z) = \begin{cases} E(0)\,e^{-ikz} & \text{for } z < 0,\\ E(L)\,e^{ik(z-L)} & \text{for } z > L.\end{cases} \quad (8)$$

Hence we arrive at the following boundary conditions

$$\begin{aligned}E'(0) &= -ikE(0),\\ E'(L) &= ikE(L),\end{aligned} \quad (9)$$

which, together with Eqs. (7), define a boundary value problem (BVP). It is important to note that this BVP does not have unique solutions: if $E(z)$ is a solution then $\rho E(z)$ is also a solution for any complex number $\rho \neq 0$.

The H-projection discussed in the following section will remove this non-uniqueness.

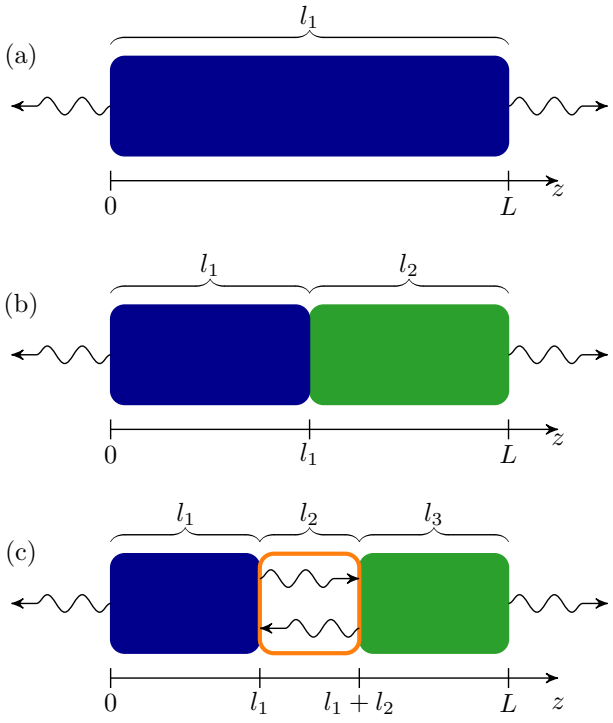


FIG. 2. (a) Single-section laser with open boundaries. (b) Two-section laser structure with open outer boundaries and (blue (dark grey) and green (medium grey)) two active-medium sections. (c) Three-section laser structure with open outer boundaries, comprising of two (blue (dark grey) and green (medium grey)) active-medium sections separated by a (white with orange (light grey) perimeter) vacuum gap.

III. THE H-PROJECTION

The purpose of the H-projection is to reduce the dimensionality of the two first-order ODEs (7) from four real dimensions to two real dimensions. We define the H-projection as a map from $\mathbb{C}^2$ to the extended complex plane $\hat{\mathbb{C}} = \mathbb{C} \cup \{\infty\}$ as follows:

$$H(h_1, h_2) = \begin{cases} h_1/h_2 & \text{for } h_2 \neq 0, \\ \infty & \text{for } h_2 = 0, \end{cases} \tag{10}$$

where h_1 and h_2 are complex numbers. While H is non-invertible, it removes the non-uniqueness discussed in Sec. II A in the sense that $H(\rho h_1, \rho h_2) = H(h_1, h_2)$ for any complex number $\rho \neq 0$. The H-projection corresponds to the concept of homogeneous (or projective) coordinates in the context of complex projective geometry [2].

Using the H-projection we now introduce the dimensionless function $\mathcal{Z}(z) \in \hat{\mathbb{C}}$ via

$$\mathcal{Z}(z) = H(E'(z), kE(z)) = \begin{cases} \frac{E'(z)}{kE(z)} & \text{for } E(z) \neq 0, \\ \infty & \text{for } E(z) = 0. \end{cases} \tag{11}$$

This new function allows us to to rewrite the electric field equation (7) and boundary conditions (9) as

$$\frac{d\mathcal{Z}(z)}{dz} = -k\left(\mathcal{Z}(z)^2 + \epsilon(z)\right), \tag{12}$$

$$\mathcal{Z}(0) = -i, \tag{13}$$

$$\mathcal{Z}(L) = i. \tag{14}$$

This is the second step in Fig. 1.

The BVP (12)–(14) can be used to obtain continuous solutions on z-subinterval(s) where $\mathcal{Z}(z)$ is finite (or, equivalently, where $E(z) \neq 0$). For example, we can choose to solve (12)–(14) where $\|\mathcal{Z}(z)\| \leq 1$. The corresponding BVP for $\mathcal{Z}(z)^{-1}$ can be derived as

$$\frac{d\mathcal{Z}(z)^{-1}}{dz} = k\left(1 + \epsilon(z)\mathcal{Z}(z)^{-2}\right), \tag{15}$$

$$\mathcal{Z}(0)^{-1} = i, \tag{16}$$

$$\mathcal{Z}(L)^{-1} = -i, \tag{17}$$

and used to obtain continuous solutions on z-subinterval(s) where $\|\mathcal{Z}(z)\| \geq 1$, including $\mathcal{Z}(z) = \infty$ (or, equivalently, $E(z) = 0$). Then, one can match the resulting solutions at the unit circle $\|\mathcal{Z}(z)\| = \|\mathcal{Z}(z)^{-1}\| = 1$ to construct continuous solutions valid on the entire z-interval $[0, L]$. Once a solution $\mathcal{Z}(z)$ is obtained, we can recover the original complex-valued electric field function $E(z)$ for a given $E(0)$ by integrating Eq. (11) to obtain

$$E(z) = E(0) \exp\left(k \int_0^z \mathcal{Z}(z')dz'\right). \tag{18}$$

Since switching between $\mathcal{Z}(z)$ and $\mathcal{Z}(z)^{-1}$ is cumbersome, we propose the Riemann sphere in the next section as a more elegant way of representing solutions to the BVP (7) and (9).

A. The Riemann sphere

The dimensionality reduction from (7) to (12) allows us to obtain intuitive insight into the nature of optical modes. A convenient way of visualising the extended complex plane $\hat{\mathbb{C}}$ is through the stereographic projection onto the *Riemann Sphere*, which is given by

$$(r_x, r_y, r_z) = \frac{1}{1 + |\mathcal{Z}|^2}\left(2\mathrm{Re}\left[\mathcal{Z}\right], 2\mathrm{Im}\left[\mathcal{Z}\right], |\mathcal{Z}|^2 - 1\right). \tag{19}$$

Here, (r_x, r_y, r_z) are coordinates in a three dimensional *embedding space*, and Eq. (19) restricts to a sphere of radius 1 where $r_x^2 + r_y^2 + r_z^2 = 1$. The point $\mathcal{Z} = 0$ is mapped

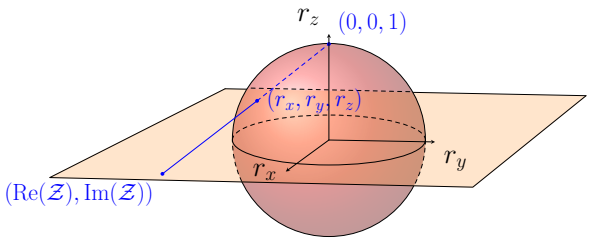


FIG. 3. Stereographic projection of a point in the extended complex plane $\hat{\mathbb{C}}$ onto the Riemann sphere embedded in $\mathbb{R}^3$ according to equation (19).

to the point $(0, 0, -1)$, while the complex infinity $\mathcal{Z} = \infty$ is mapped to the point $(0, 0, 1)$ in the embedding space. The boundary conditions $\mathcal{Z} = -i$ and i in equations (13) and (14) are mapped to points $(0, -1, 0)$ and $(0, 1, 0)$ in the embedding space, respectively. This is part of the third and the last step in Fig. 1, which is illustrated in Fig. 3. Since the Riemann sphere is a compact version of the extended complex plane, the last two steps of our formalism can be viewed as *compactification*.

B. Connection to physical quantities

Quantities of physical interest are the intensity of the complex-valued electric field $|E(z)|^2$ and the power flow given by the time-averaged Poynting vector [1, Ch.1.3],

$$\mathcal{S}(z) = \mathrm{Re}\left[\frac{i}{2\mu_0 kc} E(z)(E'(z))^*\right], \tag{20}$$

where $(E'(z))^*$ is the complex-conjugate of $E'(z)$. Using Eq. (18), we can express these quantities in terms of the $\mathcal{Z}$ function as follows

$$|E(z)|^2 = |E(0)|^2 \exp\left(2k \int_0^z \mathrm{Re}\left[\mathcal{Z}(z')\right] dz'\right), \tag{21}$$

$$\mathcal{S}(z) = \frac{1}{2\mu_0 c} |E(z)|^2 \,\mathrm{Im}\left[\mathcal{Z}(z)\right]. \tag{22}$$

The interpretation of $\mathcal{S}(z) > 0$ at a given z is that energy flows in the positive z-direction (from left to right) at this z. Since $\mathcal{S}(z) > 0$ implies $\mathrm{Im}\left[\mathcal{Z}(z)\right] > 0$, such energy flow is represented by points on the eastern hemisphere of the Riemann sphere, i.e. points around $(0, 1, 0)$. The opposite holds for $\mathcal{S}(z) < 0$.

In the following, it is convenient to introduce and work with the dimensionless electric field

$$\hat{E}(z) = \frac{E(z)}{E(0)}, \tag{23}$$

and the dimensionless Poynting vector

$$\hat{S}(z) = 2\mu_0 c \frac{\mathcal{S}(z)}{|E(0)|^2} = |\hat{E}(z)|^2 \,\mathrm{Im}\left[\mathcal{Z}(z)\right], \tag{24}$$

Note from (21) and (23) that

$$|\hat{E}(z)|^2 = \exp\left(2k \int_0^z \mathrm{Re}\left[\mathcal{Z}(z')\right] dz'\right). \tag{25}$$

IV. LOXODROMES FOR SINGLE-SECTION LASERS

Before applying the H-projection to multi-section lasers, let us first illustrate its use and introduce the basic concepts in the context of the well-known single-section Fabry-Perot laser shown in Fig. 2(a). We ignore any effects that cause spatial variation of $\epsilon(z)$ within the section, such as spatial hole-burning, and consider the simplest case of constant permittivity $\epsilon(z) = \epsilon_c$. We assume $\mathrm{Im}\left[\epsilon_c\right] < 0$, which corresponds to the case of net local gain in the laser section.

A. Fixed Point Analysis

Using the definitions

$$\mathcal{Z}_1^V(z) = -i\sqrt{\epsilon(z)}, \quad \mathcal{Z}_2^V(z) = i\sqrt{\epsilon(z)}, \tag{26}$$

we can rewrite (12) in the form of a non-autonomous [11] ODE:

$$\frac{d\mathcal{Z}(z)}{dz} = -k\left(\mathcal{Z}(z) - \mathcal{Z}_1^V(z)\right)\left(\mathcal{Z}(z) - \mathcal{Z}_2^V(z)\right), \tag{27}$$

which holds for any spatially-varying $\epsilon(z)$. In the special case of a spatially-constant $\epsilon(z) = \epsilon_c$, Eq. (27) becomes an autonomous ODE:

$$\frac{d\mathcal{Z}(z)}{dz} = -k(\mathcal{Z}(z) - \mathcal{Z}_1^F)(\mathcal{Z}(z) - \mathcal{Z}_2^F), \tag{28}$$

where

$$\mathcal{Z}_1^F = -i\sqrt{\epsilon_c}, \quad \mathcal{Z}_2^F = i\sqrt{\epsilon_c}. \tag{29}$$

We can view Eq. (28) as a planar autonomous dynamical system that evolves over z, and thus use the concepts of phase plane and linear stability to give a *qualitative* description of solutions to (28). The two points $\mathcal{Z}_1^F$ and $\mathcal{Z}_2^F$ are *fixed points*. The 'stability' of these fixed points is obtained from the complex-valued Jacobian $J(\mathcal{Z})$ which is given by,

$$J(\mathcal{Z}) = -2k\mathcal{Z}(z). \tag{30}$$

We have $\mathrm{Re}\left[\epsilon_c\right] > 0$ and $\mathrm{Im}\left[\epsilon_c\right] < 0$. Using the convention $\mathrm{Re}\left[\sqrt{\epsilon_c}\right] > 0$ results in $\mathrm{Re}\left[\mathcal{Z}_1^F\right] < 0$ and $\mathrm{Im}\left[\mathcal{Z}_1^F\right] < 0$. Using (30) we see that $\mathrm{Re}\left[J(\mathcal{Z}_1^F)\right] = -2k\mathrm{Re}\left[\mathcal{Z}_1^F\right] > 0$ and $\mathrm{Im}\left[J(\mathcal{Z}_1^F)\right] \neq 0$. Therefore $\mathcal{Z}_1^F$ acts as an unstable spiral, meaning that solutions spiral away from $\mathcal{Z}_1^F$ in the phase plane $\mathcal{Z}$. Similar arguments show that $\mathcal{Z}_2^F$ acts as a stable spiral, meaning that solutions spiral towards $\mathcal{Z}_2^F$ in $\mathcal{Z}$.

B. Loxodrome solution

We now show that the general solution to (28) has a special form known as a *loxodrome* [2, 5, 12]. To define a loxodrome formally, the concepts of *logarithmic spiral* and Möbius transformation are required. A logarithmic spiral is a curve in $\hat{\mathbb{C}}$ given by

$$Q(z) = Q_0 \exp[Wz], \tag{31}$$

where $Q_0, W \in \mathbb{C}$ and $z \in \mathbb{R}$. A Möbius transformation is a function M on $\hat{\mathbb{C}}$ of the form

$$M(p) = \frac{a_{11}p + a_{12}}{a_{21}p + a_{22}}, \tag{32}$$

where $p \in \hat{\mathbb{C}}$ and a_{ij} are complex numbers which fulfill the condition

$$a_{11}a_{22} - a_{21}a_{12} \neq 0.$$

We note that every Möbius transformation has an inverse which is also a Möbius transformation. A loxodrome is defined as a Möbius transformation of a logarithmic spiral, i.e. as $M(Q(z))$.

To obtain the general solution to (28), we consider the following Möbius transformation from $\mathcal{Z} \in \hat{\mathbb{C}}$ to $\mathcal{Y} \in \hat{\mathbb{C}}$:

$$\mathcal{Y} = \frac{\mathcal{Z} - \mathcal{Z}_1^F}{\mathcal{Z} - \mathcal{Z}_2^F} = \frac{\mathcal{Z} + i\sqrt{\epsilon_c}}{\mathcal{Z} - i\sqrt{\epsilon_c}}. \tag{33}$$

This transformation maps the fixed points $\mathcal{Z}_1^F$ and $\mathcal{Z}_2^F$ to 0 and ∞, respectively. When applied to (28), we obtain

$$\frac{d\mathcal{Y}(z)}{dz} = 2i\sqrt{\epsilon_c}\, k\, \mathcal{Y}(z). \tag{34}$$

The general solution to (34) is a logarithmic spiral in the form of (31) with $Q_0 = C$ and $W = 2i\sqrt{\epsilon_c}\, k$:

$$\mathcal{Y}(z) = C\, e^{2i\sqrt{\epsilon_c}\, kz}, \tag{35}$$

where $C \in \mathbb{C}$ is an unknown constant of integration. Applying the inverse transformation of (33), namely

$$\mathcal{Z} = i\sqrt{\epsilon_c}\, \frac{\mathcal{Y} + 1}{\mathcal{Y} - 1}, \tag{36}$$

to (35), we obtain the general solution for (28) as

$$\mathcal{Z}(z) = \sqrt{\epsilon_c}\, \frac{D\cos(\sqrt{\epsilon_c}\, kz) - \sqrt{\epsilon_c}\sin(\sqrt{\epsilon_c}\, kz)}{D\sin(\sqrt{\epsilon_c}\, kz) + \sqrt{\epsilon_c}\cos(\sqrt{\epsilon_c}\, kz)}, \tag{37}$$

where $D \in \mathbb{C}$ is an unknown constant of integration. The general solution $\mathcal{Z}(z)$ to (28), given in (37), is a Möbius transformation of a logarithmic spiral and therefore a loxodrome.

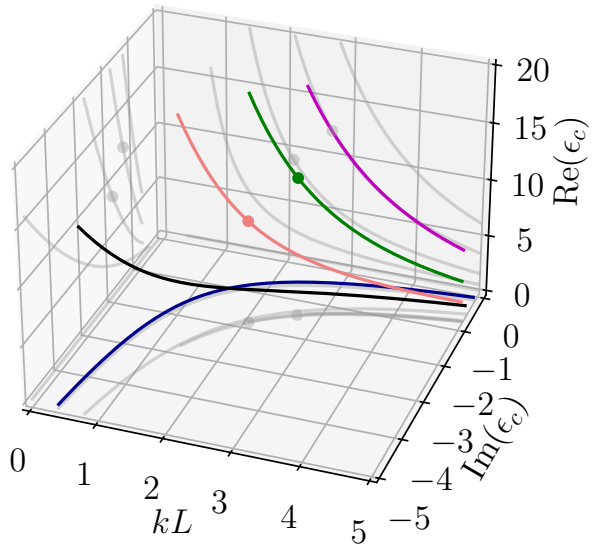


FIG. 4. Five solution branches of equation (43). The red (light grey) and green (medium grey) dots correspond to Table I. Note that the axes in this and all following figures show dimensionless quantities.

C. Boundary Conditions

We now impose boundary conditions for the single-section laser to fix the unknown constant(s) of integration, and obtain combinations of ϵ_c and kL that correspond to the *lasing modes*.

Firstly, we note from the general logarithmic spiral solution (35) that $C = \mathcal{Y}(0)$, and obtain

$$\mathcal{Y}(z) = \mathcal{Y}(0)\, e^{2i\sqrt{\epsilon_c}\, kz}, \tag{38}$$

$$\mathcal{Y}(L) = \mathcal{Y}(0)\, e^{2i\sqrt{\epsilon_c}\, kL}. \tag{39}$$

In the physically relevant case of a laser, we have $\mathrm{Re}[\epsilon_c] > 0$, $\mathrm{Im}[\epsilon_c] < 0$, and $kL > 0$. Thus, Eq. (38) describes a logarithmic spiral starting from a given $\mathcal{Y}(0)$, with two unknown parameters $\epsilon_c \in \mathbb{C}$ and $kL \in \mathbb{R}$. Condition (39) fixes ϵ_c and kL so that the spiral connects to a given $\mathcal{Y}(L)$. In other words, multiple solutions to (39) correspond to multiple *single-section lasing modes*. Transforming the boundary conditions (13) and (14) using (33), we obtain

$$\mathcal{Y}(0) = \frac{1 - \sqrt{\epsilon_c}}{1 + \sqrt{\epsilon_c}} \quad \text{and} \quad \mathcal{Y}(L) = \frac{1 + \sqrt{\epsilon_c}}{1 - \sqrt{\epsilon_c}}, \tag{40}$$

and rewrite (39) as

$$\pm 1 = \frac{1 - \sqrt{\epsilon_c}}{1 + \sqrt{\epsilon_c}}\, e^{i\sqrt{\epsilon_c}\, kL}. \tag{41}$$

We use this formula to illustrate lasing modes as a family of one-dimensional manifolds in the three-dimensional parameter space $(\mathrm{Re}\,[\epsilon_c]\,, \mathrm{Im}\,[\epsilon_c]\,, kL)$ as shown in Fig. 4.

Alternatively, we note from the general loxodrome solution (37) that $D = \mathcal{Z}(0)$, and obtain

$$\mathcal{Z}(z) = \sqrt{\epsilon_c}\,\frac{\mathcal{Z}(0)\cos(\sqrt{\epsilon_c}\,kz) - \sqrt{\epsilon_c}\sin(\sqrt{\epsilon_c}\,kz)}{\mathcal{Z}(0)\sin(\sqrt{\epsilon_c}\,kz) + \sqrt{\epsilon_c}\cos(\sqrt{\epsilon_c}\,kz)}. \quad (42)$$

Then imposing the boundary conditions (13) and (14) yields the single-section lasing modes condition

$$i = \sqrt{\epsilon_c}\frac{-i\cos(\sqrt{\epsilon_c}\,kL) - \sqrt{\epsilon_c}\sin(\sqrt{\epsilon_c}\,kL)}{-i\sin(\sqrt{\epsilon_c}\,kL) + \sqrt{\epsilon_c}\cos(\sqrt{\epsilon_c}\,kL)}. \quad (43)$$

Condition (43) is equivalent to condition (41), meaning that it fixes $\epsilon_c \in \mathbb{C}$ and $kL \in \mathbb{R}$ so that the loxodrome solution $\mathcal{Z}(z)$ connects $\mathcal{Z}(0) = -i$ and $\mathcal{Z}(L) = i$. This condition will be useful when we generalise the calculation of lasing modes to multi-section lasers.

D. Loxodromes for Single-Section Lasers

Using the tools we have introduced so far, let us now demonstrate how lasing modes in a single section laser can be represented on the Riemann sphere and on the complex $\mathcal{Z}$ plane. This will also allow us to connect loxodromes to physical characteristics such as the electric field intensity and power flow. Taking the parameter values corresponding to the red (light grey) dot in Fig. 4 (first parameter set in Table I), we obtain a solution $\mathcal{Z}(z)$ given by (42). This solution is shown in the extended complex plane $\mathcal{Z}$ in Fig. 6(a), and projected onto the Riemann Sphere in Fig. 5(a). In Fig. 6(a), we observe that the resulting loxodrome connects the boundary conditions $-i$ and $+i$ by spiralling away from the unstable fixed point $Z_1^F = -i\sqrt{\epsilon_c}$, crossing through 0, and spiraling towards the stable fixed point $Z_2^F = i\sqrt{\epsilon_c}$. Equivalently, we can observe the same behaviour on the Riemann sphere in Fig. 5(a). The electric field intensity $|E(z)|^2$ of the corresponding lasing mode can be obtained using (21). From Fig. 6(b), we can see the this field intensity has three maxima and two minima inside the laser section.

Similarly, taking the parameter values corresponding to the green (medium grey) dot in Fig. 4 (second parameter set in Table I), another example of a loxodrome is shown in the extended complex plane $\mathcal{Z}$ in Fig. 7(a), and projected onto the Riemann sphere in Fig. 5(b). The key difference is that, in this instance, the loxodrome spirals through infinity, not through 0. The electric field intensity of the corresponding lasing mode has four maxima and three minima inside the laser, and it vanishes at the central minimum, where $E(L/2) = 0$, or equivalently $\mathcal{Z}(L/2) = \infty$.

To provide a deeper geometrical intuition of the loxodromes on the Riemann sphere as seen in Fig. 5 , we include green (medium grey) circles which are representatives of the family of all circles on the sphere going through the two fixed points $\mathcal{Z}_1^F$ and $\mathcal{Z}_2^F$. In addition, we include red (light grey) circles which are representatives of the family of circles that are perpendicular to the green (medium grey) circles. Mathematically, these red (light grey) circles correspond to an *orthogonal pencil of cycles* with centres $\mathcal{Z}_1^F$ and $\mathcal{Z}_2^F$ as explained in [5]. The defining property of the loxodrome curve is that it crosses each family of circles at a fixed angle [2].

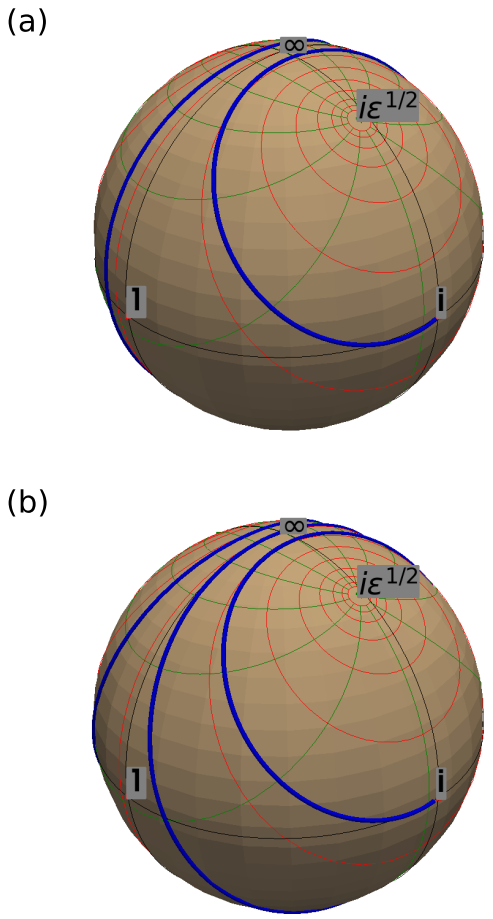


FIG. 5. Blue (dark grey) lines show the loxodrome solutions $\mathcal{Z}(z)$ projected onto the Riemann sphere using equation (19). The parameter sets for the two panels (a) and (b) are given in Table I. The red (light grey) and green (medium grey) circles are the orthogonal pencils with centers $\mathcal{Z}_1^F = -i\sqrt{\epsilon_c}$ and $\mathcal{Z}_2^F = i\sqrt{\epsilon_c}$.

Let us now connect the lasing modes of a single-section laser to the power flow $\hat{S}(z)$ inside the laser as defined in (24). For the two examples studied above, this is shown in Figs. 6(c) and 7(c), respectively. In both cases we find $\hat{S}(0) < 0$ and $\hat{S}(L) > 0$, which corresponds to outgoing light at either end. In addition, $\hat{S}(z)$ in-

Parameters	For Figs. 5(a) and 6	For Figs. 5(b) and 7
kL	2.1	2.7
ϵ_c	$9.0709 - 1.9521i$	$12.2368 - 1.5171i$
$\mathcal{Z}_2^F = -\mathcal{Z}_1^F$	$0.3222 + 3.0290i$	$0.2164 + 3.5048i$

TABLE I. Parameters used for Figs. 5, 6 and 7.

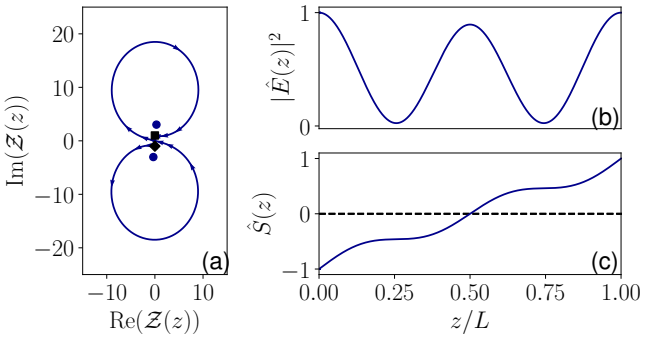


FIG. 6. (a) Parametric plot of the loxodrome solution $\mathcal{Z}(z)$ on the complex plane; the boundary conditions $+i$ and $-i$ are indicated by a square and a diamond, respectively; the blue (dark grey) dots indicate the fixed points Z_1^F and Z_2^F. Panels (b) and (c) show the corresponding electric field intensity profile $|\hat{E}(z)|^2$ and power flow profile $\hat{S}(z)$. The parameter set is given in the first column of Table I.

creases monotonously with increasing z, and we have $\hat{S}(L/2) = 0$.

V. COMPOSITE LOXODROMES FOR MULTI-SECTION LASERS

Following the use of the H-projection for the single-section Fabry-Perot laser, our next aim is to obtain solutions to the BVP (12)-(14) in the case of a multi-section laser. This will be realised through a composition of different Möbius transformations, one for each section, in a way that is reminiscent of the transfer matrix approach [13].

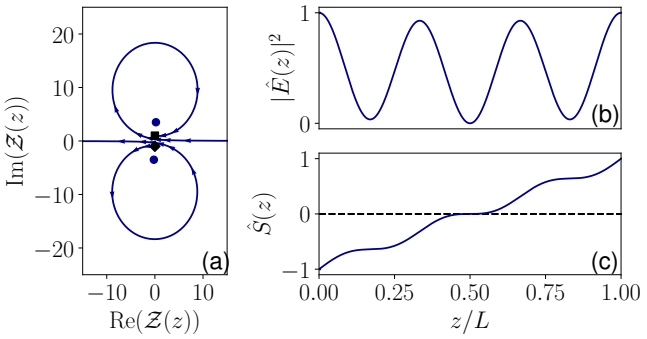


FIG. 7. As Fig. 6 but for parameter set given in second column of Table I.

To be specific, we consider an n-section laser of the total length L, and use l_j to denote the length of section j, so that $l_1 + \ldots l_n = L$. We assume that permittivity $\epsilon(z)$ in Eq. (12) is a piecewise-constant function of z, and use ϵ_j to denote constant permittivity in section j. Furthermore, we use z_j to denote the position of the boundary between sections j and $j+1$, with $z_0 = 0$ and $z_n = L$.

A. Composition of Möbius Transformations

To make the calculation of multi-section loxodromes efficient, we introduce the following convenient notation for Möbius transformations. For a 2×2 complex matrix

$$A = \begin{pmatrix} a_{11} & a_{12} \\ a_{21} & a_{22} \end{pmatrix}, \tag{44}$$

we define the corresponding Möbius transformation $[A]$ as follows

$$[A](p) = \begin{bmatrix} a_{11} & a_{12} \\ a_{21} & a_{22} \end{bmatrix}(p) \equiv \frac{a_{11}p + a_{12}}{a_{21}p + a_{22}}. \tag{45}$$

Note that the representation of Möbius transformations is not unique. In particular a matrix cA defines the same Möbius transformation as A for any complex $c \neq 0$. Furthermore, we note that

$$([A] \circ [B])(p) = [AB](p), \tag{46}$$

meaning that the composition of Möbius transformations $[A]$ and $[B]$ is a Möbius transformation $[AB]$ given by the matrix product AB.

Using this notation, we rewrite transformation (33) for section j in the form

$$\mathcal{Y}_j(z) = \begin{bmatrix} 1 & i\sqrt{\epsilon_j} \\ 1 & -i\sqrt{\epsilon_j} \end{bmatrix}(\mathcal{Z}_j(z)), \quad z \in [z_{j-1}, z_j]. \tag{47}$$

Similarly, general solution (38) in $\mathcal{Y}$ for section j can be written in the form

$$\mathcal{Y}_j(z) = \begin{bmatrix} e^{2i\sqrt{\epsilon_j}\,k(z-z_{j-1})} & 0 \\ 0 & 1 \end{bmatrix}(\mathcal{Y}_j(z_{j-1})). \tag{48}$$

Next, we invert (47) to rewrite general solution (42) in $\mathcal{Z}$ for section j as a composition of Möbius transformations

$$\mathcal{Z}_j(z) = \begin{bmatrix} i\sqrt{\epsilon_j} & i\sqrt{\epsilon_j} \\ 1 & -1 \end{bmatrix} \circ \begin{bmatrix} e^{2i\sqrt{\epsilon_j}\,k(z-z_{j-1})} & 0 \\ 0 & 1 \end{bmatrix} \circ \begin{bmatrix} 1 & i\sqrt{\epsilon_j} \\ 1 & -i\sqrt{\epsilon_j} \end{bmatrix}(\mathcal{Z}_j(z_{j-1})). \tag{49}$$

In this way, we obtain n individual loxodromes, $\mathcal{Z}_1(z), \ldots, \mathcal{Z}_n(z)$, one for each section j. The electromagnetic field boundary conditions at the interface of two sections with different permittivities require continuity in the electric field and its first derivative [1]

$$E_j(z_j) = E_{j+1}(z_j) \quad \text{and} \quad E'_j(z_j) = E'_{j+1}(z_j).$$

According to (11), this translates into continuity in $\mathcal{Z}$ alone

$$\mathcal{Z}_j(z_j) = \mathcal{Z}_{j+1}(z_j). \tag{50}$$

We then use the interior condition (50) to concatenate individual loxodromes (49) into a continuous but typically non-smooth *composite loxodrome* $\mathcal{Z}^{comp}(z)$. It is important to note that $\mathcal{Z}^{comp}(z)$ depends on $\mathcal{Z}_1(z_0)$ and $3n$ real parameters. These real parameters can be chosen as $\mathrm{Re}(\epsilon_1), \ldots, \mathrm{Re}(\epsilon_n)$, $\mathrm{Im}(\epsilon_1), \ldots, \mathrm{Im}(\epsilon_n)$, kL and the $n-1$ ratios of section lengths $kl_1 : kl_2 : \ldots : kl_n$. In Section VI we will consider a more convenient set of parameters based on different physical characteristics of the individual sections. Next, we need to ensure that such $\mathcal{Z}^{comp}(z)$ satisfies boundary conditions (13) and (14). Thus, we impose $\mathcal{Z}^{comp}(0) = \mathcal{Z}_1(z_0) = -i$ together with $\mathcal{Z}^{comp}(L) = \mathcal{Z}^{comp}(z_n) = i$, and use (46) to arrive at

$$\begin{aligned} i = &\begin{bmatrix} \cos(\sqrt{\epsilon_n}\, kl_n) & -\sqrt{\epsilon_n}\sin(\sqrt{\epsilon_n}\, kl_n) \\ \frac{\sin(\sqrt{\epsilon_n}\, kl_n)}{\sqrt{\epsilon_n}} & \cos(\sqrt{\epsilon_n}\, kl_n) \end{bmatrix} \circ \\ &\cdots \\ &\circ \begin{bmatrix} \cos(\sqrt{\epsilon_1}\, kl_1) & -\sqrt{\epsilon_1}\sin(\sqrt{\epsilon_1}\, kl_1) \\ \frac{\sin(\sqrt{\epsilon_1}\, kl_1)}{\sqrt{\epsilon_1}} & \cos(\sqrt{\epsilon_1}\, kl_1) \end{bmatrix} (-i). \end{aligned} \tag{51}$$

This complex condition fixes all $3n$ real parameters to ensure that $\mathcal{Z}^{comp}(z)$ satisfies (13) and (14). Its multiple solutions correspond to multiple *multi-section lasing modes*.

In practice, we avoid varying all $3n$ real parameters simultaneously and construct $\mathcal{Z}^{comp}(z)$ as follows. We fix the $3n$ real parameters using realistic values, start the first loxodrome from $-i$ when $z = z_0 = 0$ so that the first boundary condition (13) is satisfied, and proceed with loxodrome concatenation as described above. The result is a composite loxodrome $\mathcal{Z}^{comp}(z)$ whose endpoint $\mathcal{Z}^{comp}(L)$ lies somewhere on an extended complex plane. Next, we want to relax as few of the $3n$ real parameters as possible to ensure that $\mathcal{Z}^{comp}(L)$ moves to the point $\mathcal{Z} = i$, so that the second boundary condition (14) is satisfied too. Since $\mathcal{Z} = i$ is a single point on the extended complex plane, meaning it is of codimension-two, at least two of the $3n$ real parameters need to be varied simultaneously to achieve $\mathcal{Z}^{comp}(L) = i$. In this way we obtain a family of composite loxodromes that solve the BVP (12)–(14) with a piecewise-constant $\epsilon(z)$. A particular advantage of this approach is that it can be extended to any continuous spatially-varying permittivity profile $\epsilon(z)$ by using a suitable piecewise-constant approximation of $\epsilon(z)$ with sufficiently large n. Finally, the electric field intensity and power flow of the corresponding multi-section lasing modes are obtained using (21) and (24), respectively.

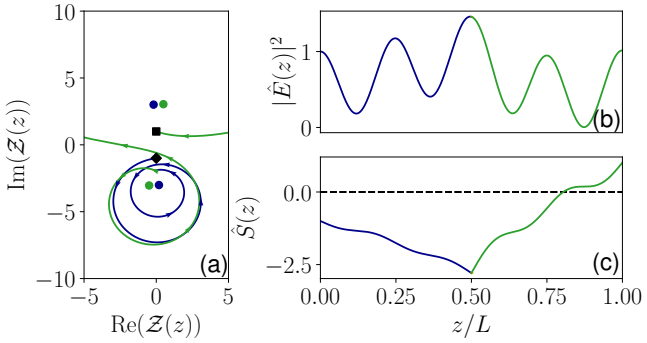


FIG. 8. (a) Parametric plot of the loxodrome solution $\mathcal{Z}(z)$ on the complex plane; the boundary values of $+i$ and $-i$ are indicated by a square and a diamond, respectively; the blue (dark grey) and green (medium grey) dots indicate the fixed points for sections 1 and 2 respectively. Panels (b) and (c) show the corresponding electric field intensity profile $|\hat{E}(z)|^2$ and power flow profile $\hat{S}(z)$. Blue (dark grey) curves and green (medium grey) curves denote $\mathcal{Z}(z)$ for the first and second sections respectively. The parameter values are given in the first column of Table II.

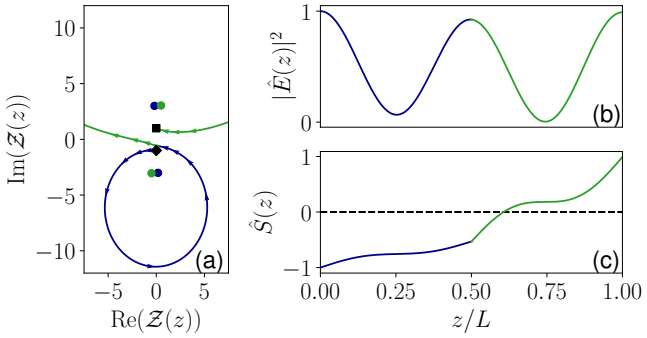


FIG. 9. The same as Fig. 8 but for parameter values given in the second column of Table II.

B. Two-section Laser

Before we move on to a three-section laser, we briefly discuss a two-section laser that is characterised by six real parameters. A two-section laser problem has four fixed points, two for each section, which we denote $\mathcal{Z}^F_{j,1} = -i\sqrt{\epsilon_j}$ and $\mathcal{Z}^F_{j,2} = i\sqrt{\epsilon_j}$, where $j = 1, 2$.

First, we concatenate two loxodromes using the left-boundary condition (13) and the interior condition (50). Then, we vary two real parameters kL and $\mathrm{Im}(\epsilon_1)$ to satisfy the right-boundary condition (14). The ensuing composite loxodromes reveal two types of *lasing modes*: *Gain-Gain* (GG) lasing modes and *Absorption-Gain* (AG) lasing modes.

Parameters	For Fig. 8 (AG)	For Fig. 9 (GG)
kL	4.2437	2.112
$kl_1 : kl_2$	1 : 1	1 : 1
ϵ_1	$9.0 + 1.1138i$	$9.0 - 0.8575i$
ϵ_2	$9.0 - 3.0i$	$9.0 - 3.0i$
$\mathcal{Z}^F_{1,2} = -\mathcal{Z}^F_{1,1}$	$-0.1853 + 3.006i$	$0.1427 + 3.0036i$
$\mathcal{Z}^F_{2,2} = -\mathcal{Z}^F_{2,1}$	$0.4934 + 3.0402i$	$0.4934 + 3.0402i$

TABLE II. Parameters used for Figs. 8 and 9 with the corresponding fixed points.

Parameters	For Figs. 10(a) and 11 (GNG)	For Figs. 10(b) and 12 (GNA)
kL	19.4456	20.0942
$kl_1 : kl_2 : kl_3$	10 : 1 : 10	10 : 1 : 10
ϵ_1	$9.2503 - 0.3042i$	$8.8759 - 0.3599i$
ϵ_2	1	1
ϵ_3	$9.2086 - 0.1350i$	$8.9344 + 0.2625i$
$\mathcal{Z}^F_{12} = -\mathcal{Z}^F_{11}$	$0.049995 + 3.0418i$	$0.06039 + 2.9799i$
$\mathcal{Z}^F_{22} = -\mathcal{Z}^F_{21}$	i	i
$\mathcal{Z}^F_{32} = -\mathcal{Z}^F_{31}$	$0.0223 + 3.0347i$	$-0.0439 + 2.9894i$

TABLE III. Parameters used for Figs. 11 and 12.

An example of a GG lasing mode is shown in Fig. 9 with parameter values given in Table II. This mode has two gain sections and is similar to the single-section lasing mode. The difference is that there are now two loxodrome parts, each with a different pair of fixed points. The loxodrome in section one (blue (dark grey)) spirals away from unstable $\mathcal{Z}^F_{1,1}$ towards stable $\mathcal{Z}^F_{1,2}$, and the loxodrome in section two (green (medium grey)) spirals away from unstable $\mathcal{Z}^F_{2,1}$ towards stable $\mathcal{Z}^F_{2,2}$.

An example of an AG lasing mode is shown in Fig. 8. This mode is very different from the single-section lasing mode owing to the combination of one absorbing section ($\mathrm{Im}(\epsilon_1) > 0$) and one gain section ($\mathrm{Im}(\epsilon_2) < 0$). As a consequence, the corresponding loxodrome (blue (dark grey)) spirals towards $\mathcal{Z}^F_{1,1}$, which is now stable.

C. Three-Section Laser

A three-section laser is characterised by nine real parameters, and has six fixed points, two for each section, which we denote $\mathcal{Z}^F_{j,1} = -i\sqrt{\epsilon_j}$ and $\mathcal{Z}^F_{j,2} = i\sqrt{\epsilon_j}$, where $j = 1, 2, 3$. We now discuss the specific example of a three-section laser shown in Fig. 2(b), where the two outer sections with local gain or absorption are separated by a section with a vacuum gap. As a result we have $\epsilon_2 = 1$, and thus equation (51) becomes

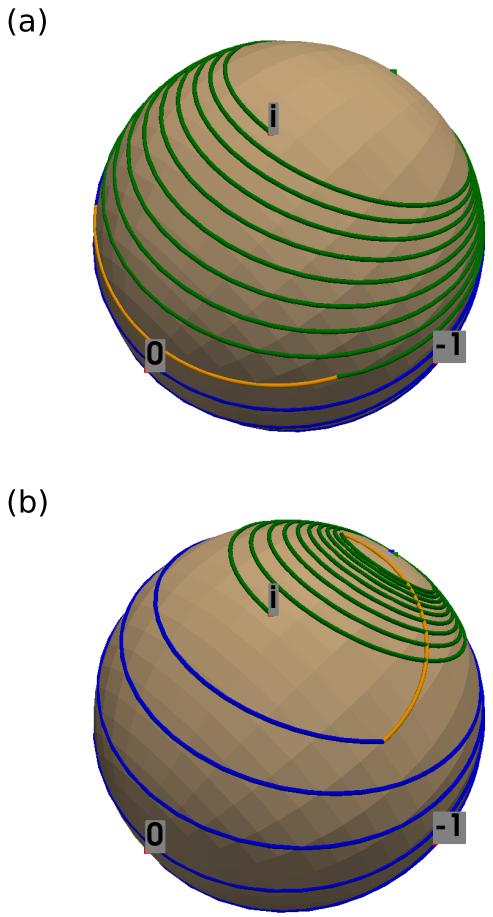


FIG. 10. Blue (dark grey), orange (light grey) and green (medium grey) lines show the loxodrome solutions of the three section laser in the respective sections 1,2, and 3 projected onto the Riemann sphere. The parameter sets for the two panels (a) and (b) are given in Table III.

$$i = \begin{bmatrix} \cos(\sqrt{\epsilon_3}kl_3) & -\sqrt{\epsilon_3}\sin(\sqrt{\epsilon_3}kl_3) \\ \frac{\sin(\sqrt{\epsilon_3}kl_3)}{\sqrt{\epsilon_3}} & \cos(\sqrt{\epsilon_3}kl_3) \end{bmatrix} \circ \begin{bmatrix} \cos(kl_2) & -\sin(kl_2) \\ \sin(kl_2) & \cos(kl_2) \end{bmatrix} \circ \begin{bmatrix} \cos(\sqrt{\epsilon_1}kl_1) & -\sqrt{\epsilon_1}\sin(\sqrt{\epsilon_1}kl_1) \\ \frac{\sin(\sqrt{\epsilon_1}kl_1)}{\sqrt{\epsilon_1}} & \cos(\sqrt{\epsilon_1}kl_1) \end{bmatrix} (-i). \quad (52)$$

Similarly to the two-section laser, we expect two fundamentally different types of lasing modes (solutions to (52)). For net local gain in both outer sections, which corresponds to $\mathrm{Im}[\epsilon_1] < 0$ and $\mathrm{Im}[\epsilon_3] < 0$, we expect *Gain-Neutral-Gain* (GNG) lasing modes. On the other hand, for net local gain in one outer section and net local absorption in the other outer section, which cor-

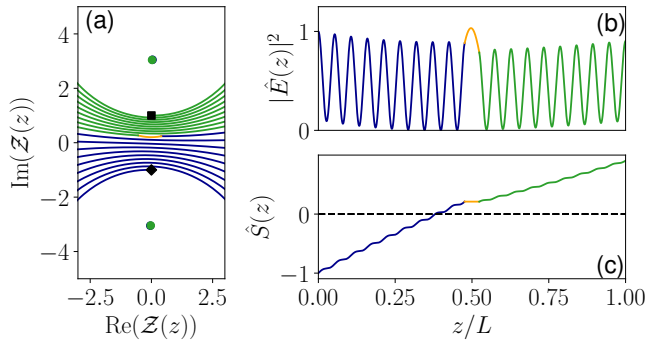


FIG. 11. (a) Parametric plot of the loxodrome solution $\mathcal{Z}(z)$ on the complex plane; the boundary values of $+i$ and $-i$ are indicated by a square and a diamond, respectively; the blue (dark grey) and green (medium grey) dots indicate the fixed points for sections 1 and 3 respectively. Panels (b) and (c) show the corresponding electric field intensity profile $|\hat{E}(z)|^2$ and power flow profile $\hat{S}(z)$. The colour scheme follows from Fig. 10 and the parameter set is given in the first column of Table III

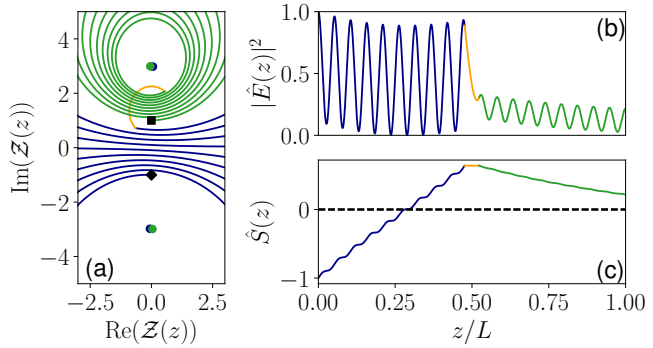


FIG. 12. As Fig. 11 but for parameter set given in second column of Table III.

responds to $\mathrm{Im}[\epsilon_1] < 0$ and $\mathrm{Im}[\epsilon_3] > 0$ or vice versa, we expect *Gain-Neutral-Absorbing* (GNA) lasing modes and *Absorbing-Neutral-Gain* (ANG) lasing modes, respectively.

Using the values in Table III, an example of a GNG lasing mode is shown in Fig. 10(a) and Fig. 11(a). The parameters are chosen to match the green (medium grey) dot in Fig. 14. The dynamics is governed by the fixed-point structure in each section. $\mathcal{Z}(z)$ starts out at $-i$ and spirals away from $\mathcal{Z}_{11}^F$ towards $\mathcal{Z}_{12}^F$ on a loxodrome trajectory (blue (dark grey) curve). At $z = l_1$ the vacuum gap causes $\mathcal{Z}(z)$ to follow a circle until $z = z_2$ (orange (light grey) curve). In the third section, $\mathcal{Z}(z)$ again follows a loxodrome that spirals towards $\mathcal{Z}_{32}^F$ to finish at $\mathcal{Z}(L) = i$ (green (medium grey) curve). The overall picture in this case is similar to the single-section Fabry Perot case, since both sections 1 and 3 carry net gain. This is also illustrated in Fig. 11(c), which shows that the power flow increases in sections 1 and 3. The corresponding electric field intensity is shown in Fig. 11(b). The field intensities in sections 1 and 3 are of comparable magnitude.

An example of a GNA lasing mode is shown in Fig. 10(b) and Fig. 12 for parameters that match the blue (dark grey) dot in Fig. 14. Since section 3 is now absorbing, $\mathcal{Z}(z)$ (green (medium grey) curve) spirals away from $\mathcal{Z}_{32}^F$ before reaching the final point $\mathcal{Z}(L) = i$. As a consequence, the power flow now has a maximum in the inner vacuum section as shown in Fig. 12(c). Fig. 12(b) indicates that the electric field intensity in section 3 is significantly smaller than in section 1.

VI. HOMOGENEOUSLY BROADENED MEDIA AND CUSP POINTS

Here, we revisit single-section and three-section lasers from a different perspective. Our aim is to reformulate the problem in terms of parameters that correspond to typical physical characteristics of the active-medium, such as gain, or population inversion, and population-induced refractive-index change. For clarity of exposition, we consider a homogeneously broadened two-level active medium. For consistency with the single-mode constant-intensity approximation used in Section II, we assume constant population inversion in each section.

To characterise permittivity $\epsilon_j \in \mathbb{C}$ in section j by the active-medium population inversion N_j in section j we use [14–16],

$$\epsilon_j = n_{b,j}^2 + \frac{N_j}{\Delta_j + i}, \tag{53}$$

where $n_{b,j} \in \mathbb{C}$ is the background refractive index in section j, N_j is the population inversion in section j, and

$$\Delta_j = \frac{k - k_{0,j}}{\gamma_{P,j}},$$

quantifies the population-induced refractive-index change in section j; $c\,k_{0,j}$ is the two-level active-medium transition frequency and $c\,\gamma_{P,j}$ is the active-medium polarisation decay in units inverse second. As a result, the $3n$ independent real parameters listed below Eq. (50) are replaced by $(6n+1)$ independent parameters: $\mathrm{Re}(n_{b,1}), \ldots, \mathrm{Re}(n_{b,n}), \mathrm{Im}(n_{b,1}), \ldots, \mathrm{Im}(n_{b,n}), N_1, \ldots, N_n, k_{0,1}, \ldots, k_{0,n}, \gamma_{P,1}, \ldots, \gamma_{P,n}, k, l_1, \ldots, l_n$.

A significant reduction in the number of parameters is obtained if we restrict ourselves to particular laser structures, where each section either is a vacuum section, or contains the same type of an active medium with the possibility of different population inversions in different non-vacuum sections. Then, the parameters $n_{b,i}$, $k_{0,i}$, and $\gamma_{P,i}$ are the same for all non-vacuum sections, and we denote these global parameters by n_b, k_0, and γ_P, respectively. As a result, the population-induced refractive-index change Δ_j is also the same in each non-vacuum

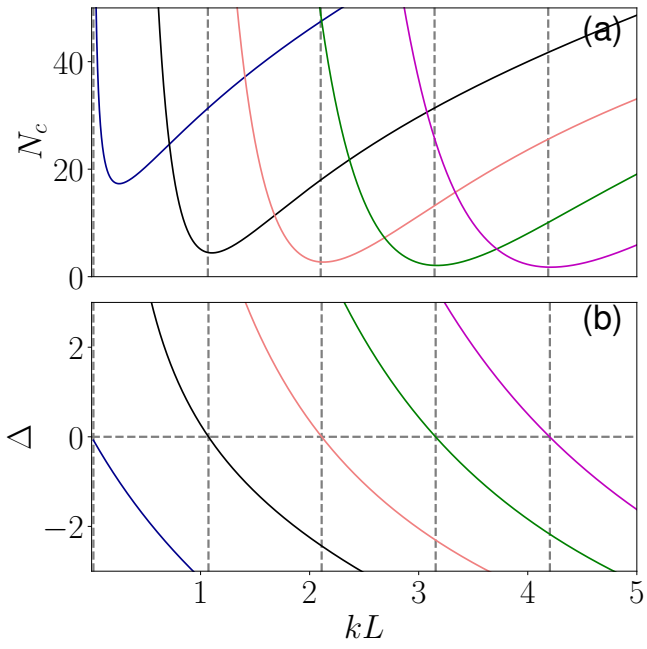


FIG. 13. Five solution branches of lasing modes in a single section laser using equation (43) with (55) for $n_b = 3 + 0.13i$ projected to the (kL, N_c) plane (a) and (kL, Δ) plane (b).

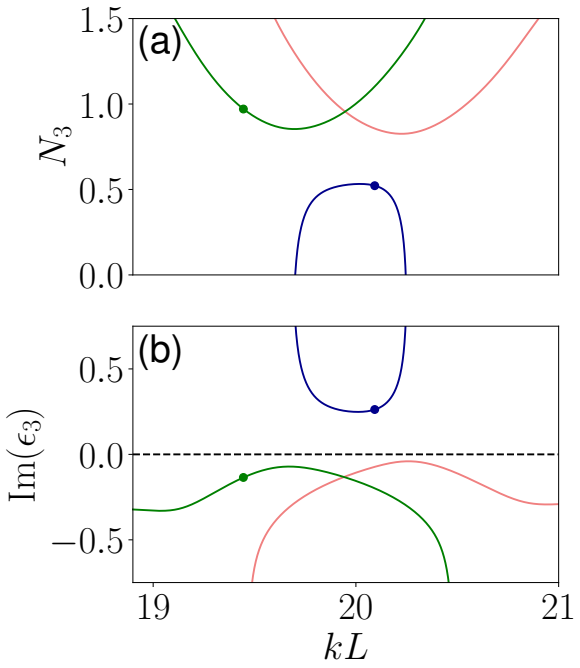


FIG. 14. (a) Solution branches of equation (52) using (56)–(58) for $kl_1 : kl_2 : kl_3 = 10 : 1 : 10$, $n_b = 3 + 0.13i$ and $N_1 = 1.15$ in the (kL, N_3) plane. (b) Corresponding $\mathrm{Im}(\epsilon_3)$ plot using equation (58). The green (medium grey) and blue (dark grey) dots indicate the values used in Table III.

section, and we denote it by Δ. Then, Eq. (53) becomes

$$\epsilon_j = \begin{cases} n_b^2 + \frac{N_j}{\Delta + i} & \text{for non-vacuum sections} \\ 1 & \text{for vacuum sections} \end{cases}. \tag{54}$$

Furthermore, we consider k and Δ to be independent parameters, which further simplifies the problem. In other words, in a laser with m non-vacuum sections, we have $m + n + 3$ real independent parameters: $\mathrm{Re}(n_b)$, $\mathrm{Im}(n_b)$, $N_1, \ldots, N_m$, Δ, kL and the $n-1$ ratios of section lengths $kl_1 : kl_2 : \ldots : kl_n$. In the following, in order to compare our results to the results in [16], we allow kL, Δ and the population inversions $N_1, \ldots, N_m$ to vary, while keeping the other parameters fixed.

A. Single-Section Laser

In the case of a single-section laser, the permittivity is given by

$$\epsilon_c = n_b^2 + \frac{N_c}{\Delta + i}. \tag{55}$$

Using (55) in the complex equation (43) with a fixed n_b provides two real conditions for the three real parameters Δ, N_c and kL. The resulting one-dimensional solution branches of lasing modes are shown in Fig. 13. Fig. 13(a) shows the variation of N_c for the various branches as a function of kL. These solution branches correspond to the lines shown in Fig. 4, and the two figures are related via equation (55).

B. Three Section Laser

Let us now reconsider the three section laser from Section V C in the case of homogeneous broadening. The permittivities in each section are then given by,

$$\epsilon_1 = n_b^2 + \frac{N_1}{\Delta + i}, \tag{56}$$

$$\epsilon_2 = 1 \tag{57}$$

$$\epsilon_3 = n_b^2 + \frac{N_3}{\Delta + i}. \tag{58}$$

where N_1 and N_3 are the population inversion parameters of sections 1 and 3, respectively. We choose our parameters (see figure captions) to facilitate comparison with [16].

Using (52) along with (56)-(58), we obtain the solution branches of lasing modes as shown in Fig. 14. We note that the red (light grey) and green (medium grey) branches in Fig. 14(a) are similar to branches in the single section laser as shown in Fig. 13. Fig. 14(b) shows that in these cases $\mathrm{Im}(\epsilon_3)$ is negative and therefore section 3 has net local gain. These branches therefore correspond to GNG lasing modes. However, there also exists a different type of branch, as illustrated by the blue (dark grey) lines in Fig. 14 with an inverted shape and at lower values of N_3. It has *positive* $\mathrm{Im}(\epsilon_3)$ corresponding to net local absorption in section 3 (Fig. 14(b)) and therefore

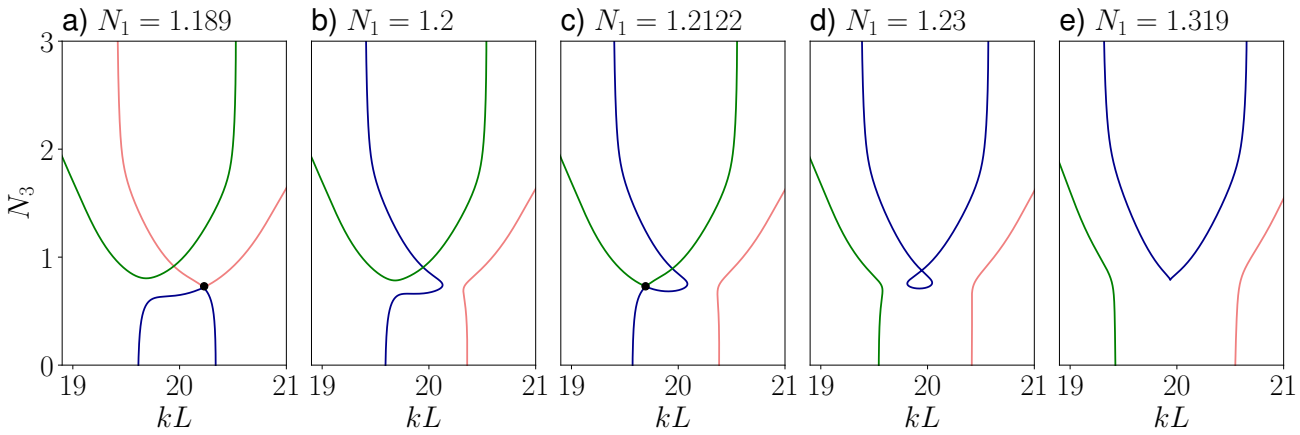


FIG. 15. Solution branches as in Fig. 14(a) for different values of N_1 indicated in each panel. Branch merge points are shown with a black dot.

this lasing mode is of the GNA type. This qualitative difference in the branches relates back to our observations in Section V.C where we differentiated solutions with net local gain and absorption in section 3. More specifically, the green (medium grey) dots in Fig. 14 correspond to the parameters of Figs. 10(a) and 11, and the blue (dark grey) dots to those of Figs. 10(b) and 12.

It is now interesting to observe, how Fig. 14(a) changes under variation of a third parameter N_1. This is illustrated in Fig. 15. These plots reveal a number of interesting phenomena, which we now discuss in detail.

To start off, consider the transition from $N_1 = 1.15$ in Fig. 14(a) to $N_1 = 1.189$ in Fig. 15(a). We see that the red (light grey) and blue (dark grey) branches meet at a special point, which we call a *branch merge point*. An enlarged version of the area around this critical point is shown in Fig. 16(a) and a plot of Δ vs. kL in (b). Taken together, this demonstrates that the red (light grey) and blue (dark grey) branches indeed meet in the three-dimensional k, N_3, Δ space. Note that there is also an apparent crossing of the green (medium grey) and red (light grey) branches at the dotted line in panel (a), which however is an artifact of this particular projection: it does not coincide with a crossing in panel (b), and therefore does not correspond to a branch merge point.

Further increase of N_1 leads to Fig. 15(b), where the branches have now a different configuration than in Fig. 14(a). In particular, both blue (dark grey) and red (light grey) branches now have GNG and GNA solutions and we observe a continuous transition between GNA and GNG lasing modes. The branches in Fig. 15(b) correspond to the threshold boundary discussed in [16, Fig.2].

As we increase N_1 further, we obtain another branch merge point, shown in Fig. 15(c). In this case, the green (medium grey) and blue (dark grey) branches merge. After the merge, the blue (dark grey) branch in Fig. 15(d) develops a peculiar loop. The green (medium grey) branch now has a continuous transition between GNA and GNG lasing modes.

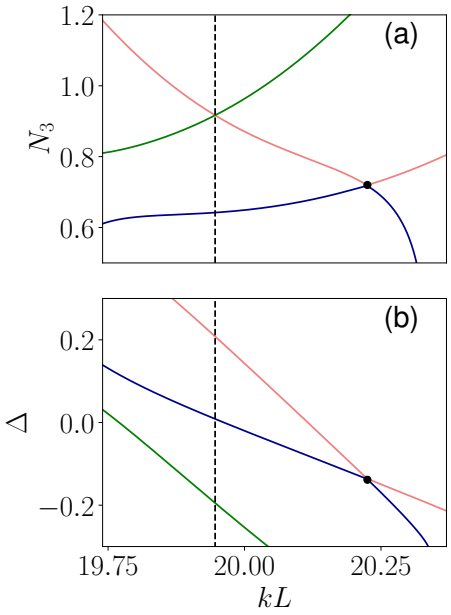


FIG. 16. (a) Enlarged version of Fig. 15(a) close up to the branch merge point (black dot). (b) Corresponding (kL, Δ) diagram.

Finally, the loop in the blue (dark grey) branch transforms into a *cusp singularity* as shown in 15(e). This is shown in greater detail in Fig. 17, where we compare the situation slightly before (a), at (b) and after (c) the appearance of the cusp singularity. We see that at the critical value of N_1, the characteristic loop in panel (a) disappears, and the blue (dark grey) curve becomes non-smooth with a sharp edge in panel (b). Upon further increase of N_1, this edge smooths out as shown in panel (c). This cusp point can be identified with an *exceptional point* at lasing threshold discussed in [16]. In the formalism from that paper, suitably defined complex "eigenvalues" are associated with individual modes, and excep-

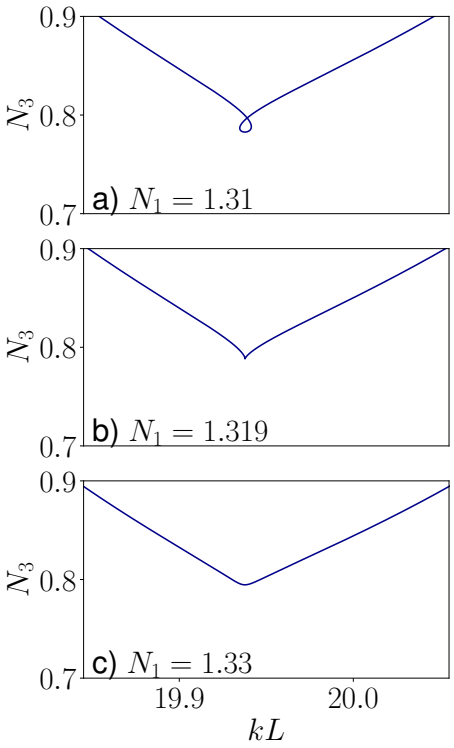


FIG. 17. Magnified solution branch close to cusp singularity for values near Fig. 15(e).

tional points are defined by a degeneracy of two such modes.

C. Cusp Point in a Two Section Laser

The overall phenomenology of branches described in the previous section for three-section lasers, is also present in the case of two-section lasers, albeit at higher values of kL. To confirm this, Fig. 18 shows the solution branches of lasing modes for a two-section laser with sections of lengths $kl_1 : kl_2 = 1 : 1$ and homogeneous broadening given by

$$\epsilon_1 = n_b^2 + \frac{N_1}{\Delta + i}, \tag{59}$$

$$\epsilon_2 = n_b^2 + \frac{N_2}{\Delta + i}. \tag{60}$$

Fig. 18(a) and (b) show the merging of two branches analogous to Fig. 15 (a) and (c), respectively. Similarly Fig. 18(c) represents a cusp point as previously shown in Fig. 18(e).

VII. CONCLUSION

We have investigated the solution space of lasing modes in open boundary multisection lasers with different complex permittivities in each section. Using suitable mathematical projections, the solutions are conveniently visualized as paths on the Riemann sphere, which start at the point $-i$ and finish at $+i$. The paths are a continuous concatenation of loxodromes, where each section corresponds to an individual loxodrome. The mathematical formalism to obtain explicit solutions for the lasing modes involves the use of Möbius transformations. This method is generally applicable to any number of sections with a different constant permittivity ϵ_c, including piecewise-constant approximations of continuously-varying permittivity profiles $\epsilon(z)$.

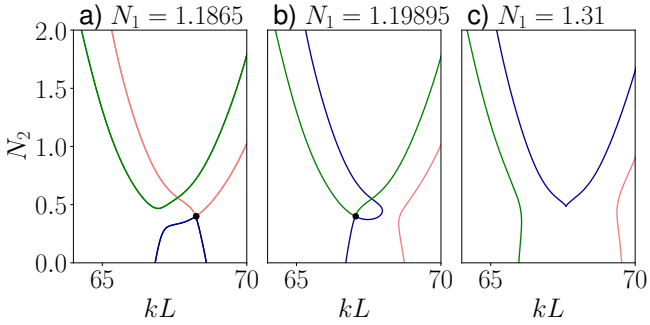


FIG. 18. Solution branches for a two-section laser with $kl_1 : kl_2 = 1$ and $n_b = 3 + 0.13i$ for different values of N_1. Branch merge points are shown with a black dot.

The formalism allows us to explore different types of solutions and the connections among them. In particular, the three section laser exhibits GNG (Gain-Neutral-Gain) and GNA (Gain-Neutral-Absorbing) solutions, which interact in a non-trivial way. In the homogeneously broadened case, we found that two types of critical points exist. The first type are *branch merging points*, where two solution branches merge. This allows for a continuous connection between GNG and GNA solutions. The second type are *cusp points* which cause the emergence of a characteristic loop in a branch and are analogous to exceptional points at threshold from [16]. Very similar behaviour is observed in the two-section laser.

[1] A. Yariv and P. Yeh, *Photonics: optical electronics in modern communications*, Vol. 6 (Oxford University Press New York, 2007).
[2] T. Needham, *Visual complex analysis* (Oxford University Press, 1998).
[3] C. Cohen-Tannoudji, B. Diu, F. Laloe, and B. Dui, Quantum mechanics (2 vol. set) (2006).
[4] M. Born and E. Wolf, *Principles of optics: electromag-*

netic theory of propagation, interference and diffraction of light (Elsevier, 2013).
[5] V. V. Kisil and J. Reid, in *Topics in Clifford Analysis* (Springer, 2019) p. 313.
[6] S. Hansmann, IEEE Journal of Quantum Electronics **28**, 2589 (1992).
[7] S. O'Brien, A. Amann, R. Fehse, S. Osborne, E. P. O'Reilly, and J. M. Rondinelli, JOSA B **23**, 1046 (2006).
[8] E. Kapon, J. Katz, and A. Yariv, Optics letters **9**, 125 (1984).
[9] W. W. Chow and S. W. Koch, *Semiconductor-laser fundamentals: physics of the gain materials* (Springer Science & Business Media, 1999).
[10] M. Sargent III, M. Scully, and W. Lamb, *Laser Physics* (Addison-Wesley, 1974).
[11] The system is non-autonomous owing to non-autonomous terms $\mathcal{Z}_1^V(z)$ and $\mathcal{Z}_2^V(z)$ with prescribed dependence on z.
[12] J. J. Monzón, A. G. Barriuso, L. L. Sánchez-Soto, and J. M. Montesinos-Amilibia, Physical Review A **84**, 023830 (2011).
[13] M. Davis and R. O'Dowd, IEEE Journal of Quantum Electronics **30**, 2458 (1994).
[14] H. Haken, *Laser light dynamics*, Vol. 1 (North-Holland Amsterdam, 1985).
[15] L. Ge, Y. D. Chong, and A. D. Stone, Physical Review A **82**, 063824 (2010).
[16] M. Liertzer, L. Ge, A. Cerjan, A. D. Stone, H. E. Türeci, and S. Rotter, Physical Review Letters **108**, 173901 (2012).